SANDIA REPORT
SAND2009-5857
Unlimited Release
Printed September 2009

RF/Microwave Properties of Nanotubes and Nanowires: LDRD Project 105876 Final Report

Mark Lee, Clark Highstrete, Julia W.-P. Hsu, David Scrymgeour

Prepared by
Sandia National Laboratories
Albuquerque, New Mexico 87185 and Livermore, California 94550

Sandia is a multiprogram laboratory operated by Sandia Corporation,
a Lockheed Martin Company, for the United States Department of Energy's
National Nuclear Security Administration under Contract DE-AC04-94AL85000.

Issued by Sandia National Laboratories, operated for the United States Department of Energy by Sandia Corporation.

Available to DOE and DOE contractors from
U.S. Department of Energy
Office of Scientific and Technical Information
P.O. Box 62
Oak Ridge, TN 37831

Telephone: (865) 576-8401
Facsimile: (865) 576-5728
E-Mail: reports@adonis.osti.gov
Online ordering: http://www.osti.gov/bridge

Available to the public from
U.S. Department of Commerce
National Technical Information Service
5285 Port Royal Rd.
Springfield, VA 22161

Telephone: (800) 553-6847
Facsimile: (703) 605-6900
E-Mail: orders@ntis.fedworld.gov
Online order: http://www.ntis.gov/help/ordermethods.asp?loc=7-4-0#online

SAND2009-5857
Unlimited Release
Printed September 2009

RF/Microwave Properties of Nanotubes and Nanowires: LDRD Project 105876 Final Report

Mark Lee, Clark Highstrete
Semiconductor Materials & Device Sciences Department

Julia W. P. Hsu
Surface & Interface Sciences Department

David Scrymgeour
Photonics Microsystems Technology Department

Sandia National Laboratories
Albuquerque, NM 87185

Abstract

LDRD Project 105876 was a research project whose primary goal was to discover the currently unknown science underlying the basic linear and nonlinear electrodynamic response of nanotubes and nanowires in a manner that will support futureefforts aimed at converting forefront nanoscience into innovative new high-frequency nanodevices. The project involved experimental and theoretical efforts to discover and understand high frequency (MHz through tens of GHz) electrodynamic response properties of nanomaterials, emphasizing nanowires of silicon, zinc oxide, and carbon nanotubes. While there is much research on DC electrical properties of nanowires, electrodynamic characteristics still represent a major new frontier in nanotechnology. We generated world-leading insight into how the low dimensionality of these nanomaterials yields sometimes desirable and sometimes problematic high-frequency properties that are outside standard model electron dynamics. In the cases of silicon nanowires and carbon nanotubes, evidence of strong disorder or glass-like charge dynamics was measured, indicating that these materials still suffer from serious inhomogeneities that limit there high frequency performance. Zinc oxide nanowires were found to obey conventional Drude dynamics. In all cases, a significant practical problem involving large impedance mismatch between the high intrinsic impedance of all nanowires and nanotubes and high-frequency test equipment had to be overcome.

Contents

1. Introduction

Carbon nanotubes (CNTs) and semiconductor nanowires (SNWs) are predicted to have unique and desirable high-frequency characteristics arising from quantum correlations, ballistic transport, and Luttinger liquid statistics unique to pure low-dimensional nanostructures. While there exist extensive efforts to characterize and exploit DC electrical properties of such nanomaterials, even the most fundamental rf/microwave properties of CNTs and SNWs remain nearly unexplored and certainly undeveloped. One of the major upcoming frontiers in nanomaterial research will be in high-frequency properties and eventual applications. To open this frontier will require a focused effort to measure and understand the fundamental electrodynamics of CNTs and SNWs across the range of frequencies relevant to communication, computation, radar, remote sensing, *etc*. (*i.e.*, MHz to THz). Only after the electrodynamic physics is sufficiently well understood can truly innovative applications, such as extremely fast, power-efficient, frequency-agile oscillators/detectors based on novel ballistic transport, or resonant chemical sensors be realistically developed. The goal of this LDRD project was to discover the new science and the foundational knowledge required before creation of innovative applications can begin.

2. AC Conductance of Doped Silicon Nanowire Arrays

Modern nanomaterials such as semiconductor nanowires are thought to have novel electrodynamic properties that are relevant to both fundamental nanomaterial physics and applications in high-speed electronics and sensors. For example, recent reports of DC ballistic transport characteristics in Ge/Si and InAs nanowires [*1*,*2*] suggest that such materials may have extremely fast, very low dissipation microwave response beyond the limit of conventional Drude transport. The sensitivity of the DC electrical properties of various nanowires to molecules adsorbed on their surfaces [*3*] also raises the question of whether similar AC conductance changes exist and can be exploited for chemical sensor purposes. Although there exists a large body of research on nanowire DC electrical properties, as well as attempts to prototype potential high frequency nanowire devices, [*4*] relatively little is known about the fundamental microwave electrodynamic response of nanowires. One reason for this is that, by virtue of its relatively long length and small

cross-sectional area, an individual nanowire presents a very high impedance, typically 10 kΩ to 1 MΩ, compared to the 50 Ω impedance of all microwave test equipment and the 377 Ω impedance of free space, so the interaction between a nanowire and the electromagnetic field is very small and usually produces a signal below instrumental background.

To circumvent this limitation, we have measured broadband microwave conductance spectra of silicon nanowires (SiNWs) assembled into arrays of 11 to > 10^4 nanowires. By using a relatively large number of SiNWs and confining the electromagnetic field within the CPW to maximize overlap with the nanowires, excellent signal levels and a very high degree of systematic reproducibility were achieved. This allowed us to accurately extract the conductance spectra of the SiNW arrays from the combined CPW/SiNW system across a broad frequency range of 0.5 to 50 GHz. The complex AC conductance of the SiNW arrays exhibited a sub-linear power law increase with frequency that is consistent with behavior found universally in disordered electronic systems. [*5,6*]

Doped crystalline SiNWs were synthesized by vapor-liquid-solid growth using phosphine (n-type) and trimethylboron (p-type) as the dopant gases. The P:Si and B:Si inlet gas flow ratios were 2 x 10^{-3} and 2 x 10^{-2}, respectively. The SiNWs were grown with an average length of 7 μm and average diameter of approximately 50 nm with variation of roughly 50% about the mean and possessed a native oxide surface layer. Two techniques were utilized to measure AC conductance: one for arrays consisting of < 500 to > 10^4 SiNWs and the other for arrays of 11 to < 200 SiNWs. I n the first technique, broadband microwave coplanar waveguides (CPWs) were fabricated with 20 nm Ti and 200 nm Au evaporated on 0.5 mm thick fused quartz substrates with 3 μm gaps between the

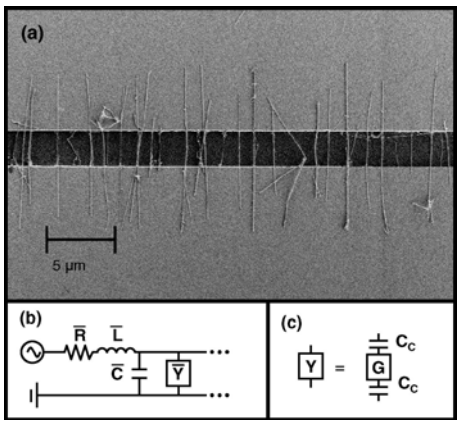

Figure 2.1. (a) Scanning electron microscope (SEM) image of a CPW segment with SiNWs assembled across an electrode gap between the center signal electrode and one ground electrode. The other electrode gap (not shown) was assembled similarly. (b) Circuit element transmission line model for a CPW with shunt admittance per unit length *Y* due to the addition of SiNWs. (c) Simple circuit model for the total admittance *Y* with complex conductance *G* coupled capacitively *C* to the CPW.

center signal and adjacent ground electrodes. Using SiNWs suspended in deionized water, arrays consisting of approximately 500 to over 10^4 SiNWs were then assembled by ac dielectrophoresis (ACDEP) [*7*] across the electrode gaps of several CPWs (the "test" CPWs), as in Figure 2.1(a), while others on the same substrate remained bare (the "control" CPWs). No additional metallization or annealing was done.

The substrates were mounted in a darkened cryogenic probe station where complex reflection and transmission coefficients (*S* parameters) [*8*] were measured with a vector network analyzer from 0.5 to 50 GHz at several temperatures between 4 and 293 K. A room temperature measurement was taken in the atmosphere and all other measurements were taken in 10^{-5} Torr vacuum after baking overnight at 395 K. Each substrate included CPWs made for impedance calibration designed with identical transverse dimensions and characteristic impedance to the test and control CPWs. The NIST-developed multiline through-reflect-line method [*9*] and StatistiCAL software were used to accurately calibrate the measurements at each temperature.

The SiNW array conductance is directly related to a change in the test CPW propagation constant *k*, calculated from *S* parameters [*10*] measured before and after ACDEP. In practice, it is more reliable to compare *k* from the test and control CPWs measured alongside each other at the same stage of the experiment (*i.e.*, same sample mounting and calibration). The variation in *k* for the test and control CPWs measured prior to ACDEP and the control CPWs after ACDEP (measured alongside the assembled test CPWs) quantify the CPW uniformity and measurement reproducibility. This variation in *k* was found to be less than 1% at all frequencies and provides an estimate of the systematic error of the experiment. For an array of 500 SiNWs, the signal to systematic error ratio ranged from approximately unity at lower frequencies to 10 at higher frequencies. For arrays of 10^4 SiNWs, it ranged from approximately 100 at low frequency to 1000 at higher frequencies.

The bare CPWs are treated as standard transmission lines with distributed series resistance *R*, inductance *L*, and shunt capacitance *C* per unit length. [*8*] The SiNW array conductance is modeled by the addition of a distributed admittance per unit length *Y* as in Fig. 2.1(b), calculated from the *S* parameters of the test and control CPWs. The array is modeled as a continuous distribution because the spacing of the SiNWs (< 1 μm) is very

small relative to the wavelengths involved (λ > 3 mm). *Y* then represents a sum of individual nanowire contributions over a unit length scale on the order of a wavelength. The approximation is then made that this averaged *Y* does not vary over the length *l* of the CPW, *i.e.*, that the SiNW array distribution is uniform over a length scale $\lambda < d < l$ (when $\lambda < l$). The oxide layer of the SiNWs produces a DC contact resistance in excess of 1 GΩ, so *Y* is modeled as a complex conductance *G* coupled capacitively to the CPW as in Fig. 2.1(c). The admittance data of the SiNW arrays confirmed the capacitive coupling which, when subtracted, resulted in a complex conductance *G* that increased sublinearly with frequency as f^s,where $s \approx 0.3$ and satisfied the Kramers-Kronig relation.

To more accurately fit the data, while accounting for known DC conductance in the SiNWs, the data were then fit with the SiNW array conductance given by:

$$G(f) = G_{DC} + A[\cos(s\pi/2) - i\sin(s\pi/2)]\, f^s \qquad (2.1)$$

Conductance data for all SiNW arrays measured, n-type and p-type, clearly showed sublinear frequency dependent conductance, with *s* in the range 0.25-0.45. The accuracy of fit parameters is affected not only by signal strength relative to systematic errors but also by spectral fluctuations at higher frequencies due to variations in array uniformity. These factors contributed to an uncertainty in *s* of < 20%. Estimating the DC conductance from the microwave spectrum is particularly dependent on the low frequency data, which has the lowest signal and highest error of the spectrum. Consequently only highly dense and uniform arrays with a G_{DC} value large enough to be distinguishable from zero relative to the AC conductance at the lowest measured frequency could generate extrapolated DC

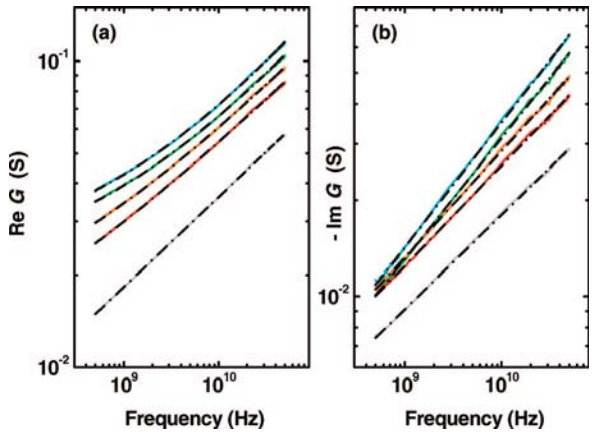

Figure 2.2. (a) Real and (b) negative imaginary parts of the SiNW array conductance at several temperatures for an n-type sample consisting of approximately 10^4 SiNWs. The top four curves are taken in vacuum at 4 K (blue), 100 K (green), 200 K (orange), and 293 K (red) from top to bottom. The bottom curve (gray) is taken at 293 K in atmosphere. The dashed curves (black) were calculated by fitting SiNW array data with the circuit model of Fig. 2.1(c) and *G*(*f*) from Eq 1.1. Values of *s* obtained were 0.39 (4 K), 0.38 (100 K), 0.33 (200 K), 0.31 (293K), and 0.30 (atmosphere).

conductance estimates.

The $G(f)$ spectra, measured in atmosphere at 293 K and in vacuum at several temperatures, of an array consisting of approximately 10^4 n-type SiNWs are shown in Fig. 2.2. The high signal and excellent uniformity of this sample provided the highest accuracy in fit parameters achieved. The conductance exhibits sublinear frequency dependence under all conditions with the exponent s increasing slightly from 0.30 in atmosphere to 0.39 at 4 K in vacuum. We can estimate average SiNW parameters by naively dividing the admittance by the number of nanowires. This produces an average value for the individual contact capacitance of 0.6 fF, in reasonable agreement with a classical estimate of 0.7 to 3 fF. The individual SiNW capacitances for all of the samples were found to be approximately equal. Similarly dividing G_{DC} yields DC resistivity estimates of 0.018, 0.020, 0.035, 0.060, and 3.5 Ω·cm, for 4 K, 100 K, 200 K, 293 K, and ambient temperature, respectively. The room temperature vacuum value of 0.06 Ω·cm is an order of magnitude larger than that expected from four-point resistance measurements [*11*] of similarly grown SiNWs. This may be partially explained by the increased systematic error at lower frequencies. Additionally, it was found that the arrays formed by ACDEP contained many SiNWs of smaller diameter than those measured in Ref 11. These smaller SiNWs may have higher resistivity due to increased surface effects.

For all of the n-type samples, as in Fig. 2.2, the magnitudes of Re G and -Im G across the measured frequency range increased significantly following bake-out under vacuum and as temperature was lowered to 4 K. Alternatively, for the p-type arrays, Re G and -Im G decreased monotonically upon bake-out and cooling. The changes in conductance upon bake-out suggest that adsorbates from atmosphere alter the carrier density and/or distribution in the SiNWs, effectively enhancing p-type conduction and diminishing n-type. The temperature dependence of the n-type and p-type samples is generally consistent with dc conductivity in bulk silicon doped above and below the metal-insulator transition, respectively. However, the sublinear frequency dependence of $G(f)$ is not consistent with the conventional Drude ac conduction seen in bulk doped silicon from dc up to terahertz frequencies

Conductivity spectra showing sublinear frequency dependence have been reported in a wide variety of seemingly unrelated electronic systems, whose only common feature is

strong microscopic disorder. [*5,6*] Like the SiNW arrays these systems have conductances that satisfy the Kramers-Kronig relation and exhibit weak dependence of the exponent *s* on temperature. However, the systems are generally noncrystalline whereas the SiNWs studied were predominantly single crystal and exhibited sublinear frequency dependent conduction at all temperatures. Additionally, the exponent range found for the SiNW arrays, $0.25 < s < 0.45$, is significantly lower than the range, $0.6 < s < 1.0$, reported for the vast majority of disordered systems. [*6*] In the theoretical treatment of this universal disordered conductance behavior, the statistical properties of the local mobility or potential distribution determine the exponent *s*. Although knowledge of *s* does not uniquely specify the underlying statistical physics, it may help rule out classes of distributions and ultimately aid in developing models for the disorder, analogous to what has been done for $1/f$ noise. [*12*] The distinct material properties and range of *s* for the SiNW arrays suggest that they may have a distinct class of disorder mechanism compared to bulk systems.

It is therefore of interest to consider the origin of the disorder. There are two possibilities: (1) macroscopic disorder from statistical variations of electronic properties within the ensemble, such as individual nanowire resistivity and coupling capacitance, dislocations, and nanowire crossings and (2) microscopic electronic disorder in the individual SiNWs. To further investigate the origin of the disorder, a second measurement technique was utilized which is more sensitive to arrays of fewer SiNWs but limited to smaller arrays, lower signal, and higher systematic error. As before, multiple calibration CPWs were fabricated together with test and control measurement structures. Here however, the measurement structures consisted of CPWs with a 2 μm gap interrupting the center conductor. Systematic error, again estimated from measurements of bare test (pre-ACDEP) and control (pre- and post-ACDEP) structures, ranged from approximately 1% at lower frequencies to 10% at higher frequencies due to the reflective nature of the test structures. Arrays consisting of 11 to approximately 200 n-type SiNWs were assembled by ACDEP across the 110 μm wide center conductor gap of several test structures and microwave measurements were made in atmosphere. The difference in admittance of the bare control and assembled test structure gap admittances, calculated from the measured *S* parameters, yielded the SiNW array admittance.

Signal to systematic error was limited at lower frequencies by SiNW conductance and at higher frequencies by systematic error. For the 11 SiNW array, signal to systematic error ranged from approximately 1 to 5, while for the 200 SiNW array it ranged from approximately 10 to 100. The spectra again indicated sublinear frequency dependence not attributable to conventional Drude conduction and were fit with the conductance model of Fig. 2.1(c) and Eq. 2.1. Conductance spectra for arrays of 11 to over 10^4 n-type SiNWs measured by the two techniques are plotted together in Fig. 2.3. The exponent values obtained for these arrays also fell in the range $0.25 < s < 0.45$. Since s is essentially independent of the number of SiNWs N forming the array across greater than three orders of magnitude and between two different measurement geometries, it would be surprising for s to be strongly dependent on N for $N < 11$. This result suggests that the sublinear conductance results from electronic disorder in the individual SiNWs rather than among the SiNWs forming an array.

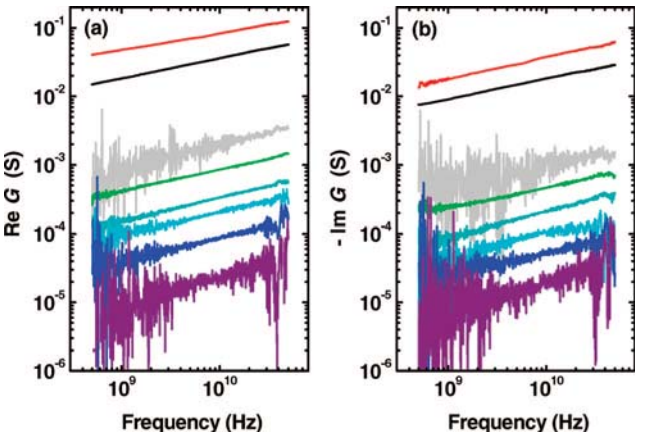

Figure 2.3. (a) Real and (b) negative imaginary parts of the conductance of various SiNW arrays measured by the two techniques discussed in the text. The arrays consisted of, from bottom to top, approximately 11 (purple), 23 (blue), 50 (light blue), 100 (blue-green), 200 (green), 500 (gray), 10000 (black), and 50000 (red) n-type SiNWs. Values of the exponent s obtained from data fits (not shown) were 0.44, 0.34, 0.30, 0.38, 0.32, 0.35, 0.30, and 0.31 respectively.

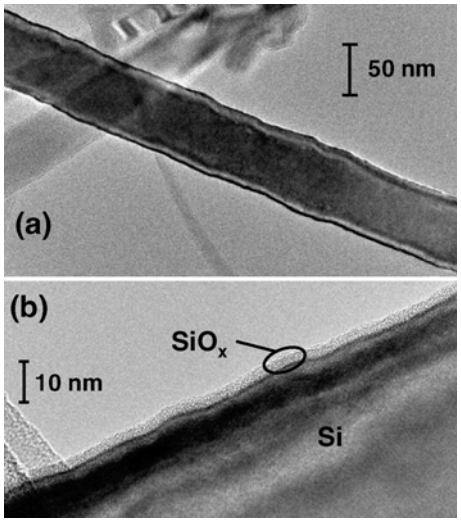

Figure 2.4. TEM images of typical n-type SiNWs showing (a) the overall surface roughness and (b) detail of the Si/SiO_x interface.

While the SiNWs measured are not small enough to be one-dimensional in a quantum sense, their large surface-tovolume ratio makes them highly susceptible to surface effects, as seen in the SiNW conductance changes between atmosphere and vacuum. If the disorder is indeed microscopic in

origin, a possible source is suggested by the transmission electron microscope (TEM) images in Fig. 2.4. The images show the Si/SiO_x interfaces of typical SiNWs accompanied by considerable roughness. It has been shown that Si/SiO_x interface roughness correlates with interface state density [*13*] and interface states have been predicted to cause sublinear conduction in crystalline solids. [*14*] Additionally, the disorder involved in elastic carrier scattering from a fixed interface potential should be insensitive to temperature. This is consistent with the weak variation of the exponent *s* in the SiNW array conductance from 4 K to room temperature. These observations suggest that the SiNW conductance may be dominated by disordered interface states.

3. AC Conductance of Single-wall Carbon Nanotube Arrays

The microwave electrodynamic properties of single-walled carbon nanotubes (SWCNTs) may be highly unconventional due to their one-dimensional nature in ways that are of fundamental scientific interest and could prove extremely useful in high-frequency (AC) electronics. Indeed, many of the novel properties calculated for and observed in the DC regime imply highly desirable microwave characteristics. For instance, very small parasitic capacitance [*15*] and ballistic transport [*16,17,18,19,20*] mean that CNTs could have extremely fast, very low power dissipation microwave response beyond what is achievable within diffusive Drude AC transport. Additionally, possible effects from Lüttinger liquid [*21,22*] and other unconventional electron physics unique to low-dimensional nanomaterials [*23*] may lead to further electronics innovations.

Existing AC experiments on CNTs have yielded intriguing but still unsettled results. Works on semiconducting CNT-based field effect transistors [*24,25*] and rectifiers, [*26*] as well as metallic CNTs, [27] have claimed no high-frequency roll-off attributable to dissipation in the CNT up to a range of 10 to 50 GHz. It is possible that the loss contribution from a single or small number of CNTs can be hidden by much larger, frequency-dependent instrumental and parasitic losses and noise. A report of kinetic inductance in single and bundled SWCNTs [*28*] supports non-dissipative ballistic transport, but direct measurements of microwave loss have been reported for arrays of SWCNTs [29] and for multiwalled CNTs. [*30,31*] Impedance problems stemming from

the high (> 10 kΩ) intrinsic and contact resistances of SWCNTs has also led to the use of large parallel arrays to achieve the 50 Ω impedance matching condition needed in most microwave circuits. [*32*] As high frequency electronic applications continue to evolve using CNTs as active or passive elements, it is important to develop a thorough understanding of these nanomaterials' basic AC conductance properties.

Here we report on quantitative measurements of the complex AC conductance G_{CNT} in arrays of SWCNTs at frequencies f from 0.1 to 50 GHz. Similar to Sect. 2, arrays consisting of 10^3 to 10^4 SWCNTs were measured, so that the response is from ensembles of mixed metallic and semiconducting SWCNTs rather than from a single SWCNT. Excellent signal-to-noise ratio and a very high quantitative level of systematic reproducibility were achieved using the precision calibration and de-embedding techniques described in Sect. 2 for microwave measurements on nanomaterials. Re$G_{CNT}(f)$ and Im$G_{CNT}(f)$ were obtained at each frequency from magnitude and phase data. In all samples G_{CNT} was found to scale with frequency as a sub-linear power law, *i.e.* $G_{CNT} \sim f^s$, where the exponent $s \approx 0.67$ for all arrays measured. Because Re$G_{CNT}(f)$ was non-zero, microwave power was dissipated by the CNT arrays. This sub-linear frequency dependence is inconsistent with either Drude or ballistic transport models.

SWCNT material produced by the high pressure carbon monoxide method was purchased from Carbon Nanotechnologies, Inc. (now Unidym), [*33*] who claim this process selectively produces 100% SW material. SWCNT suspensions were prepared using an ultracentrifugation purification procedure [*34*] described in detail in Ref. 10. The final purified SWCNTs were suspended in a deionized water solution with sodium cholate and sodium dodecyl sulfate as surfactants to prevent aggregation. SWCNT arrays were assembled onto broadband co-planar waveguides (CPWs) using the AC dielectrophoresis directed assembly technique [*7*] described in Sect. 2. Electron microscope images showed the arrays to be composed of ensembles of individual SWCNTs as well as numerous ropes and bundles of entangled nanotubes. The SWCNTs forming the arrays were of mixed chiralities and diameters.

To estimate the statistical distribution of SWCNT types in an array, micro-Raman measurements were performed on a separate test sample assembled using the same suspension and ACDEP conditions as for the microwave measurement samples. The data

are shown in Fig. 3.1. The observed radial breathing modes suggest that SWCNTs with chiralities of (13,0), (10,4) and (9,3) were the most abundant. [*35*] From the integrated breathing mode intensities, an estimated 60% of the SWCNTs in this array were metallic, which is consistent with the splitting in the graphene peak near 1600 cm^{-1}. An enhancement in metallic SWCNT fraction compared to the starting suspension is expected due to the higher attractive force exerted on metallic nanotubes in ACDEP. [*7*] The presence of the defect peak showed that there were a significant amount of lattice defects in these SWCNTs.

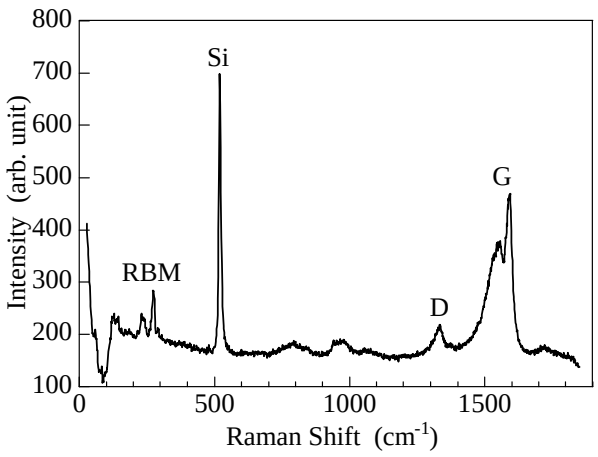

Figure 3.1. Micro-Raman spectrum of a SWCNT array assembled using the same ACDEP parameters as for the CPW samples. In addition to the substrate peak (Si), the spectrum shows two prominent radial-breathing-mode peaks (RBM), a lattice defect peak (D) and dual graphene lattice peaks (G), suggesting an approximate 60% metallic SWCNT content in these types of arrays.

The CPW electrodes consisted of 20 nm Ti and 200 nm Au evaporated on 0.5 mm thick fused quartz substrates. Two different CPW geometries were used. In the "shunt" geometry, SWCNT arrays were assembled across the two 2 μm wide gaps between center conductor and outer ground planes along the length of a CPW. In the "series" geometry, SWCNT arrays bridged a 2 μm gap interrupting the continuity of the center conductor in the middle of the CPW's length. Also, two different electrical contact conditions were used. In addition to assembling SWCNTs onto bare Au electrodes, which resulted in ohmic DC contacts, CPWs were prepared with 100 nm of silicon nitride deposited onto the Au to prevent DC contact between SWCNTs and the CPW electrodes. In these insulated arrays the CNT-to-electrode contacts are purely capacitive. The geometric and electrical contact variations required different transmission line models to extract the conductance of the CNT arrays themselves. However, the frequency dependence of the SWCNT array conductance spectra obtained was quantitatively consistent for all cases.

Measurements of the complex reflection (S_{11}) and transmission (S_{21}) parameters of the assembled CPWs were made at each frequency using a vector network analyzer.

Details of the calibration procedures are described in Ref. 10. Wafers having several measurement CPWs along with calibration structures were mounted in a cryostat / vacuum chamber outfitted with broadband microwave test access. To get quantitatively reproducible data, measurements were made in vacuum of $\leq 10^{-5}$ mbar after baking out several hours at ~ 80 °C and then cooling to ambient temperature. Experimental procedure was as follows: *S*-parameters were first measured for each CPW on a wafer prior to ACDEP assembly to verify cross-sample uniformity. SWCNTs were then assembled on several CPWs on a wafer and the *S*-parameters were re-measured. For every wafer undergoing the ACDEP process, at least one CPW on the wafer was processed alongside but without CNTs, thus establishing a control sample. Re-measurement of the control CPWs alongside the CNT-assembled CPWs monitored possible spurious processing effects and quantified systematic measurement reproducibility. The *S*-parameters of control CPWs were reproduced to < 1% precision, while CPWs with assembled CPW arrays consistently showed ~ 10% changes in *S*-parameters between post-ACDEP assembly and the original bare CPWs.

The CNT arrays' intrinsic complex conductance, G_{CNT}, at each frequency was extracted from raw *S*-parameter data using analytical procedures described thoroughly in Ref. 10. Briefly, the total admittance Y_{CNT} due to an assembled CNT array was calculated from the measured *S*-matrix difference between test and control structures by treating the CPW as a transmission line, [*8*] with the assembled nanomaterial array adding a shunt admittance per unit length or a lumped series admittance to the bare CPW. Y_{CNT} includes both G_{CNT} and the contribution from contacts. From DC current-voltage (*I*-

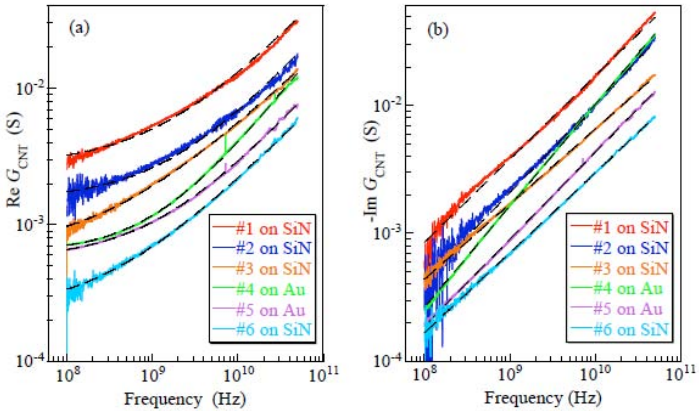

Figure 3.2. (a) Real and (b) imaginary conductance spectra for six different SWCNT arrays. In (a), the top three data curves are from Si_3N_4 insulated CPWs, the next two data curves are from CPWs with bare Au electrodes, and the bottom data curve from another Si_3N_4 insulated CPW. Contact contributions have been subtracted. The dashed black curves are fits to the conductance form of Eq. 1. For each sample, the same fitting parameter values are used to fit both real and imaginary parts.

V) and low-frequency impedance measurements, a contact resistance of 5 to 15 Ω, was found for CNTs assembled onto Au CPWs, corresponding to a rough average of order ~ 10 kΩ per CNT. A contact capacitance of 0.2 to 2 pF, of order ~ 1 fF per CNT, was found for CNTs assembled onto nitride insulated CPWs. DC *I-V* data on ohmically contacted samples showed linear behavior between ± 0.2 V, so G_{CNT} could determined by taking out the series linear contact element contributions to Y_{CNT}.

Figure 3.2 shows real and imaginary G_{CNT} as a function of frequency, *f*, for six different SWCNT arrays at room temperature in vacuum after bakeout. Four samples used Si_3N_4 to isolate the CNTs from the Au CPW electrodes and two samples had CNTs directly contacting the Au CPWs. All of these samples share the same basic array conductance spectrum: $\mathrm{Re}G_{CNT}(f)$ approaches a constant at lower frequencies and gradually crosses over to a power law frequency dependence at higher frequencies. $\mathrm{Im}G_{CNT}(f)$ is negative and shows a power law dependence at all frequencies in the measurement band. The fact that both ohmic and capacitive contacts showed the same general frequency dependence of the intrinsic CNT array conductance is evidence that the removal of contact contribution from Y_{CNT} to obtain G_{CNT} is a robust procedure. In particular, it is important to note that $\mathrm{Re}G_{CNT}$ is nonzero even in insulated samples having no DC electrical contact to the electrodes, only purely reactive contacts. This means that there is contact-independent dissipation in these arrays at all frequencies and the conduction is not ballistic.

More quantitatively, the complex conductance spectra can all be well described by Eq. 2.1, the same as for SiNWs. Fits to Eq. 2.1 are shown as dashed lines in Fig. 3.2, where for each sample both real and imaginary parts are fitted using the same G_{DC}, *A* and *s* values. G_{DC} and *A* depend on the number of CNTs in an array and range across our samples between 0.5 to 3 mS for G_{DC} (a rough average of ~ 1 μS per CNT) and ~ 0.2 to 2 $\mathrm{nS}\cdot\mathrm{sec}^s$ for *A*. The exponent *s*, on the other hand, should be intrinsic and is found to be 0.67 ± 0.08 for all samples. Hence the frequency dependent part of G_{CNT} is found to increase with frequency as a sub-linear power law using a common exponent of about 0.67. The spectra for each sample also are found to obey the Kramers-Kronig relation for a sub-linear power law conductance: $\mathrm{Im}G(f)/\mathrm{Re}G(f) = -\tan(s\pi/2)$.

The general dependence of $G_{CNT}(f)$ at various temperatures between 294 K to 4 K and on exposure to atmosphere at 294 K is shown in Fig. 3.3 for a representative array on a Si_3N_4 insulated CPW. CNT arrays assembled directly on Au showed the same trends. As temperature is decreased (in vacuum after bakeout), the frequency independent conductance G_{DC} shows a clear monotonic drop by a factor of almost three, while the magnitude A of the frequency dependent part is only weakly temperature dependent. Upon exposure to ambient atmosphere at 294 K, G_{DC} increases ~ 40% over its value at the same temperature but in vacuum. Most interestingly, the value of the exponent s is nearly independent of both temperature and atmospheric exposure within the accuracy of the measurement and fitting.

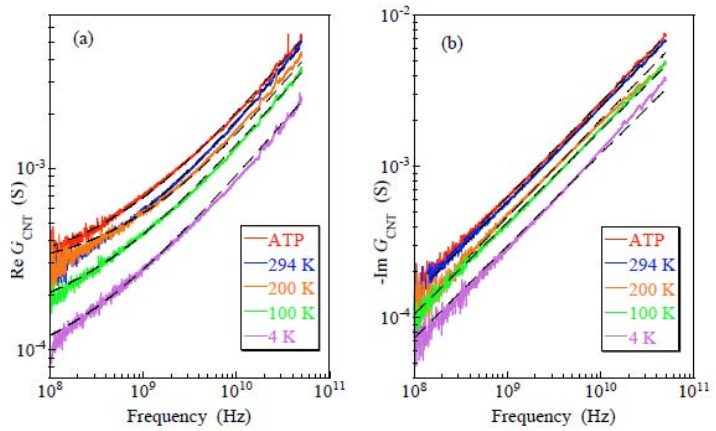

Figure 3.3. CNT array conductance of a sample assembled on one Si_3N_4 insulated CPW measured under the following conditions (from top data curve to bottom): ambient atmospheric temperature and pressure (ATP), in vacuum (after bake out) at temperatures of 294 K, 200 K, 100 K, and 4 K. The dashed black curves are fits to Eq. 2.1.

The observed G_{CNT} spectra for the CNT arrays is inconsistent with conventional Drude AC conductivity $\sigma(f) = \sigma_{DC}/(1+i2\pi f\tau)$, where τ is the scattering rate, normally seen in homogeneous metals and semiconductors. In the frequency regime $f << 1/2\pi\tau$ applicable here, the Drude model has $\mathrm{Re}\sigma(f) \approx \sigma_{DC}$ and $\mathrm{Im}\sigma(f) \propto f$. The general sub-linear frequency form and the value of s depend on the statistical distribution of the disorder and are not features specific to any particular physical origin or type of disorder. For this reason, sub-linear frequency dependencies have been reported in a wide variety of otherwise unrelated electronic systems.

In the SWCNT array system, the physical origin of the sub-linear frequency dependence is still an open question. The most significant feature of the data is that s is highly insensitive to temperature. As discussed in Ref. 6, this suggests that the disorder leading to the frequency dependence is topological, not energetic, in nature. Because the CNTs form areas with multiple crossed CNTs, such disorder possibly results from

percolative mechanisms in entwined CNT ropes, bundles, and mats, where carrier confinement and multiple conduction paths can result from physical intersections of CNTs. [*36*] Alternatively the AC conductance could also be caused by carriers locally confined along CNTs by lattice defects, whose presence is indicated by the lattice defect peak in Fig. 3.1, or physical deformations such as kinks or bends in the suspended CNTs.

4. AC Impedance Spectra of ZnO Nanowire Arrays

The future of electronic materials is showing trends away from traditional planar semiconductor geometries toward nanomaterials for many reasons: unique material geometries (*i.e.*, quasi 1-D systems), high nanomaterial quality, low power consumption, bottom up assembly and self assembly onto novel substrates, and interesting electrical properties such as ballistic transport. To exploit nanomaterials in high performance electronics, operation at high frequency (*i.e.*, > 1 GHz) becomes a primary requirement and thus fundamental high frequency properties need to be examined quantitatively. Zinc oxide has been intensively studied recently as a nanomaterial due to its ease of fabrication in a variety of nanostructured geometries and its interesting semiconducting properties. In particular, bulk ZnO has high electron mobility (up to 200 $cm^2V^{-1}s^{-1}$ at room temperature) [*37*] and theoretically high saturation velocity.[*38*] Thus, ZnO nanorods may be an excellent candidate semiconductor for high frequency nanoelectronics. The aim of this work was to study the high frequency impedance properties of solution grown ZnO nanorods, with an emphasis on trying to separate inherent sample impedance behavior from the contact properties.

Zinc oxide nanorods were grown in solution on silicon substrates using the following procedure. Si substrates were first seeded by depositing an oriented ZnO film layer. [*39*] These seeded substrates were then submerged in an aqueous growth medium containing $Zn(NO_3)_2$ and different growth modifiers, and incubated at elevated temperatures between 60 and 90 °C. Two different types of ZnO rods were grown and are distinguished by the growth modifier. The first type was grown in a neutral pH solution using diaminopropane (DAP) [*40*]; the second type was grown at high pH containing NaOH. Doping of DAP rods with gallium was carried out by adding $Ga(NO_3)_3$ into the growth solution. Some nanorod samples were then conformally coated with different

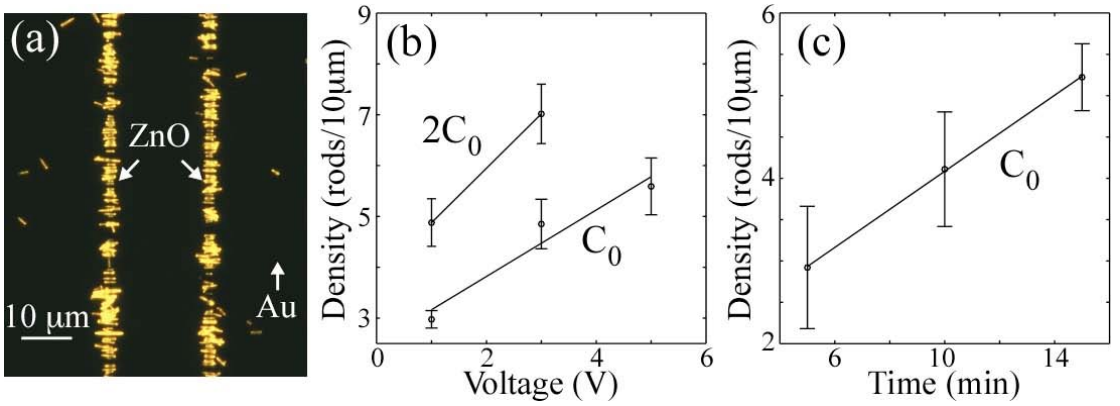

Figure 4.1: (a) Optical micrograph of a ZnO nanorod array assembled across the gaps between the center signal line and left/right ground planes of a CPW. The nanorods are luminescing under ultraviolet excitation. (b) Linear number density of nanorods in an array as a function of dielectrophoretic assembly voltage for starting concentrations C_0 and 2 C_0 of nanorods in suspension at 5 minute assembly time. (c) Linear number density of nanorods in an array as a function of dielectrophoretic assembly time at 3 V assembly voltage.

dielectrics. A TiO_2 dielectric was grown by atomic layer deposition (ALD) to a thickness of 0.8 nm as measured with spectroscopic ellipsometry. A 20 nm thick dielectric coating of cadmium sulfide (CdS) nanocrystals was grown by incubating the ZnO nanorods in an aqueous solution of 10 mM $Cd(NO_3)_2$ and 10 mM thioacetamide at room temperature for 5 to 60 minutes. [*41*]

ZnO nanorods averaging 4 μm in length were suspended in deionized water and assembled by ACDEP across the 2 μm gaps between the center signal line and ground planes of CPWs consisting of 200 nm thick gold electrodes on fused quartz substrates. A typical sample is shown in Fig. 4.1(a) with the ZnO rods luminescing yellow under ultraviolet light while the gold CPW structure is dark. The density of nanorods along the electrodes (number of nanorods per unit CPW length) can be controlled as a function of nanorod concentration in suspension, assembly time, and AC assembly voltage as shown in Fig. 4.1(b) and (c). Typical ACDEP parameters used were 5 V_{pp} at 10 MHz for 10 minutes to assemble arrays with nanorod densities between 0.5 to 5 rods/10 μm. Microwave measurements were performed using the same basic procedures described in Sects. 2 and 3.

Derivation of impedance spectra from the raw *S*-parameter data relied on conventional waveguide calibration and de-embedding techniques described in Sects. 2 and 3. As shown in Fig. 4.2(a), the assembled nanorod array was then represented by a distributed admittance per unit length *Y*, calculated from the measured *S*-parameters of

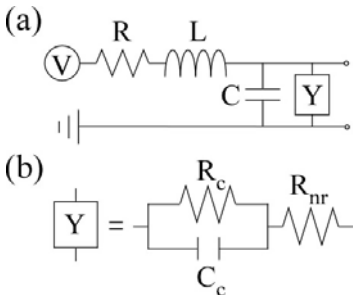

Figure 4.2: (a) CPW circuit element transmission line model with a shunt admittance per unit length Y corresponding to the average total admittance of a nanord (including both contact and inherent properties). (b) The average admittance Y of a nanorod is modeled as a simple three element RCR circuit composed of a parallel resistive and capacitive contact (R_c, C_c), in series with the inherent nanorod resistance (R_{nr}).

the test and control CPWs. Since the arrays were dense and uniformly distributed on the scale of the shortest microwave wavelength used (~ 4 mm at 50 GHz given a guided mode index of ~ 1.7 for these CPWs), Y represents an average of individual nanorod lumped admittances distributed uniformly along the CPW. With the length scale for this averaging chosen as the average nanorod spacing, Y then approximates the average admittance per nanorod, including both contact and inherent sample contributions in series. The impedance of an average nanorod element is then given by $Z = 1/Y$.

To develop a physically meaningful interpretation of the impedance vs. frequency spectra $Z(f)$, we fit the spectra to a simple physically intuitive model consisting of series contributions from the contact, modeled as a parallel resistance and capacitance (R_c, C_c), and the inherent nanorod impedance, modeled by a simple resistance (R_{nr}). This three element linear RCR model, shown schematically in Fig. 4.2(b), has as its impedance spectrum:

$$Z(f) = \left[\frac{R_c}{1 - iR_cC_c2\pi f}\right] + R_{nr} \qquad (4.1)$$

where f is the experimental frequency.

This RCR model has characteristic frequency response master curves shown in Fig. 4.3 for typical combinations of the circuit component values measured in the ZnO nanorods. In the low frequency limit, the real response approaches $\mathrm{Re}Z(f\to 0) = R_c + R_{nr}$, while the high frequency limit has $\mathrm{Re}Z(f\to\infty) = R_{nr}$. The transition between the low and high frequency regimes occurs around a frequency $f = 1/(2\pi R_cC_c)$, the characteristic contact roll-off frequency, at which $\mathrm{Im}Z$ has a maximum with value $R_c/2$. Therefore, if the frequency range of the measurement is sufficiently broad for the appropriate

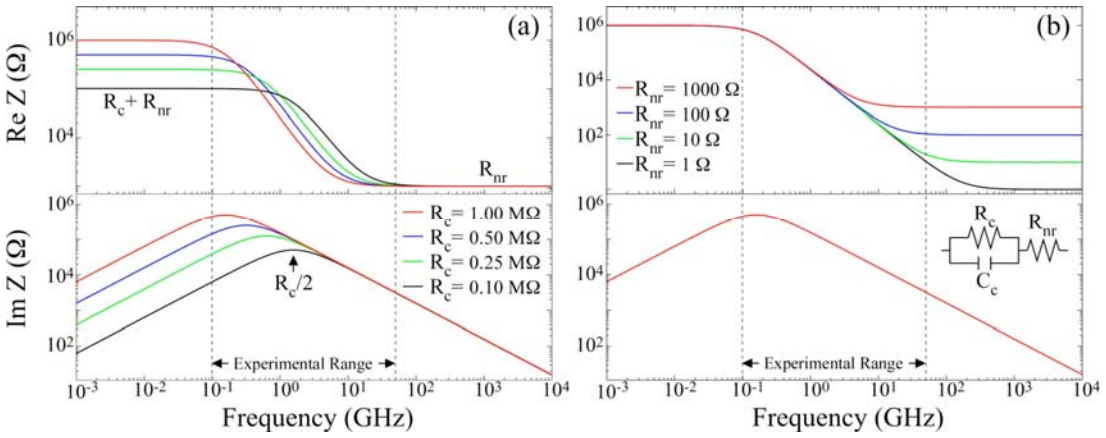

Figure 4.3. Frequency dependence impedance master curves of the *RCR* model shown in Fig. 4.2(b) calculated for typical values of C_c, R_c, and R_{nr} measured for an average ZnO nanorod. Shown in (a) is the effect of varying R_c while keeping C_c and R_{nr} constant while (b) shows varying R_{nr} keeping C_c and R_c constant. The vertical dashed lines represent the frequency range covered in this experiment. The values of components used in this calculation are R_{nr} = 1 kΩ in (a), R_c = 1.0 MΩ in (b), and C_c = 1 fF in both.

component values, comparison of high and low frequency limits in the *RCR* model permits separation of contact from inherent nanorod impedance characteristics.

Let us examine the effects of varying the circuit element parameters on the theoretical impedance curves. If the contact resistance R_c increases relative to a fixed R_{nr} as shown in Fig. 4.3(a), we see a shift in the imaginary peak to lower frequency and an increase in the low frequency value of Re$Z(f\rightarrow 0)$. Note that as R_c increases, the high frequency limit, Re$Z(f\rightarrow\infty)$ = R_{nr}, is more clearly revealed at lower measurement frequencies because of the shift of the contact roll-off to lower frequencies. If on the other hand R_{nr} is increased relative to a fixed R_c as depicted in Fig. 4.3(b), the high frequency limit Re$Z(f\rightarrow\infty)$ goes to the higher value of R_{nr} as expected and the saturation value of R_{nr}, again becomes more apparent at lower measurement frequencies. Since the contact capacitance C_c depends mostly upon the geometry of the assembled nanorods, order of magnitude changes in the physical dimensions of the nanorods are

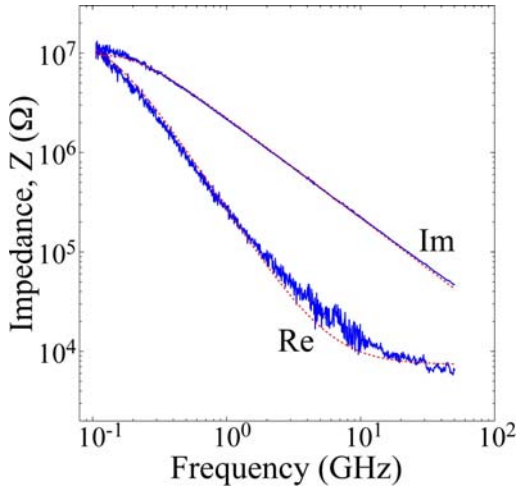

Figure 4.4. Average nanorod impedance spectrum for a typical ZnO nanorod array in blue. Red lines are the least square fits to the RCR circuit model.

required to change the contact capacitance significantly, which is not realistic experimentally. Therefore, to investigate applicability of this *RCR* model, we concentrate on variations of either the contact resistance R_c or the nanorod resistance R_{nr}.

An average nanorod impedance spectrum for a typical array of ZnO nanorods is shown in Fig. 4.4, with a least squares fit of the data to the *RCR* model of Eq. 4.1. By comparing Fig. 4.4 to the master curve of Fig. 4.3, we see that this measured impedance spectrum lies just to the right of the peak of the imaginary response at $f = 1/(2\pi R_c C_c)$. Near the highest measured frequencies, the ReZ data show a curvature inflection indicating the approach to the high frequency asymptote $\mathrm{Re}Z(f\rightarrow\infty) = R_{nr}$.

From the least squares fit of Eq. 4.1 to the data of Fig. 4.4, the extracted values for an average nanorod in the array are: $R_c = 3100 \pm 485$ kΩ, $C_c = 0.4 \pm 0.03$ fF, and $R_{nr,} = 1.4 \pm 0.3$ kΩ. We typically find R_c to be three orders of magnitude larger than R_{nr}. This gives a characteristic contact frequency $1/(2\pi R_c C_c) \sim 130$ MHz, confirming that the peak in the imaginary curve occurs close to the lowest measured frequency. The uncertainty in the fitting parameters (R_c, C_c, R_{nr}) is determined by minimizing the χ^2 (goodness of fit) value when varying a single parameter while keeping the other two fixed. For this combination of parameters, R_c has higher confidence than R_{nr}. The lower confidence in determination of the inherent nanorod resistance reflects the fact that the high contact impedance, relative to the inherent nanorod resistance, dominates the behavior of $Z(f)$ in the measured frequency range. The confidence in R_{nr} would improve with access to higher measurement frequencies and, more significantly, with the use of higher inherent resistivity (*i.e.*, more intrinsic) nanorods.

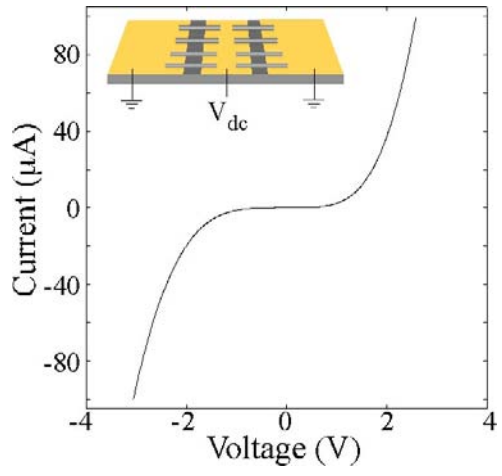

Figure 4.5: Typical DC *I-V* curve measured for a CPW structure assembled with a ZnO nanorod array. Inset shows measurement geometry.

To further investigate the applicability of the *RCR* model, we used a DC voltage bias to vary R_c at fixed R_{nr}, so as to follow Fig. 4.3(a) of the model. This was accomplished by applying a fixed DC bias between the

center conductor and the ground planes of the CPW while simultaneously measuring the AC impedance spectrum. A typical DC current-voltage (*I-V*) characteristic of a ZnO array is shown in Fig. 4.5, which exhibits obvious non-linear behavior. No attempts were made to form ohmic contacts by annealing because the gold CPW electrodes were incompatible with the annealing process. Because R_c is three orders of magnitude larger than R_{nr}, this *I-V* curve is completely dominated by contact resistance. The tangent to the *I-V* curve in Fig. 4.5 is then the R_c value at a given DC bias. This is justified because the network analyzer delivered incident power of 20 μW, corresponding to a voltage amplitude of ~ 30 mV, so the AC measurement measures the small-signal differential impedance along this *I-V*. Note that R_c decreases as DC bias increases in either polarity.

The changes in the impedance spectra with DC bias are shown in Fig. 4.6. As DC bias is increased, the low frequency asymptotic value of Re*Z* decreases as expected and the peak in Im*Z* shifts to higher frequencies as shown in Fig. 4.6(a) and (b). These changes are consistent with the master curve behavior the *RCR* model as represented in Fig. 4.3(a). Exploring the consistency more quantitatively, the maximum value of Im*Z* should equal $R_c/2$, which independently determines a value for R_c. Shown in Fig. 4.6(c) are the values of R_c determined as a function of DC bias three ways: 1) as the tangent slope from the DC *I-V* data, 2) determined from the least squares fit of the *RCR* model to the experimental complex *Z* data, and 3) extracted from the peak of the Im*Z* data. These values are in reasonable agreement, with improving agreement at higher values of DC

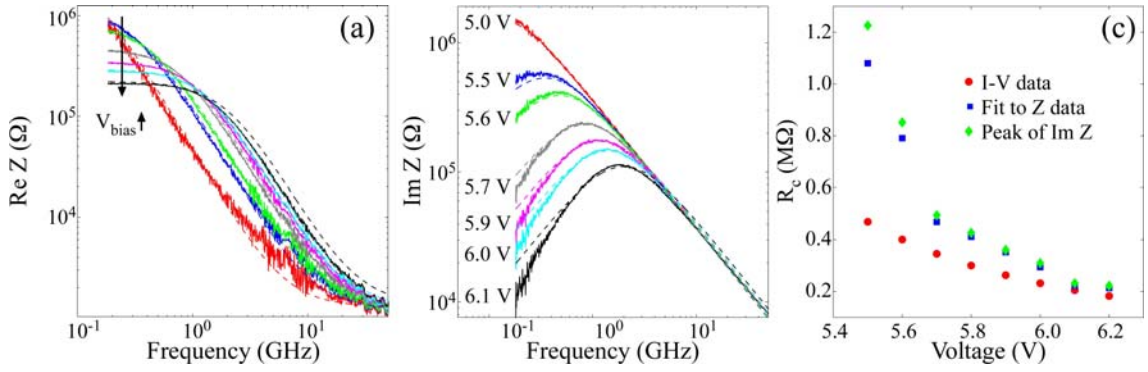

Figure 4.6. The (a) real and (b) imaginary parts of the AC impedance spectrum of a ZnO nanorod array at various values of applied DC voltage bias. (c) The contact resistance of the arrays determined by fitting the DC I-V curve (red circles), fitting the impedance data with the RCR circuit model (blue squares), and equating the peak value of the Im *Z* data with $R_c/2$ (green diamonds).

bias (*i.e.*, lower values of R_c). This consistency gives good confidence in the validity of the *RCR* model to describe the impedance spectra of the ZnO nanorod arrays.

Finally, we note that the *RCR* model analysis shows that the inherent AC impedance of an average ZnO nanorod is simply described, at least up to 50 GHz, by a resistor, R_{nr}. In particular, this means that the AC electrical conduction mechanism in a ZnO nanorod is consistent with the conventional Drude model for charge carrier response to AC fields. While this conclusion may be regarded as unsurprising, the simple Drude behavior is markedly different from what was observed for SiNWs and CNTs in Sects. 2 and 3. In those nanomaterials the AC response was found to be most consistent with the behavior expected of highly disordered electronic systems. From the perspective of AC response, the ZnO nanorods used in this experiment do not seem to suffer from a similar degree of disorder.

5. References

[1] X. Zhou, S. A. Dayeh, D. Aplin, D. Wang, E. T. Yu, Appl. Phys. Lett. **89**, 053113 (2006)

[2] G. Liang, J. Xiang, N. Kharche, G. Klimeck, C. M. Lieber, M. Lundstrom, Nano Lett. **6**, 642 (2007)

[3] A. A. Talin, L. Hunter, F. Leonard, B. Rokad, Appl. Phys. Lett. **89**, 153102 (2006)

[4] J. Xiang, W. Lu, Y. Hu, Y. Wu, H. Yan, C. M. Lieber, Nature **441**, 489 (2006)

[5] A. K. Jonscher, Nature **267**, 673 (1977)

[6] J. C. Dyre, T. B. Schroder, Rev. Mod. Phys. **72**, 873 (2000)

[7] H. A. Pohl, *Dielectrophoresis: The Behavior of Neutral Matter in Nonuniform Electric Fields* (Cambridge University Press: New York) 1978

[8] D. M. Pozar, *Microwave Engineering, 3rd ed.* (J. Wiley: Hoboken, NJ) 2005

[9] D. F. Williams, J. C. M. Wang, U. Arz, IEEE Trans. Microwave Theory Tech. **51**, 2391 (2003)

[10] C. Highstrete, Ph.D. Thesis, University of New Mexico (2008)

[11] Y. Wang, K.-K. Lew, T. Ho, L. Pan, S. W. Novak, E. C. Dickey, J. M. Redwing, T. S. Mayer, Nano Lett. **5**, 2139 (2005)

[12] P. Dutta, P. Dimon, P. M. Horn, Phys. Rev. Lett. **43**, 646 (1979)

[13] Y. Yamashita, A. Asano, Y. Nishioka, H. Kobayashi, Phys. Rev. B **59**, 15872 (1999)

[14] K. L. Ngai, A. K. Jonscher, C. T. White, Nature **277**, 185 (1979)

[15] H. M. Manohara, E. W. Wong, E. Schlecht, B. D. Hunt, P. H. Siegel, , Nano Lett. **5**, 1469 (2005)

[16] J. Kong, E. Yenilmez, T. W. Tombler, W. Kim, H. J. Dai, R. B. Laughlin, L. Liu, C. S. Jayanthi, S. Y. Wu, Phys. Rev. Lett. **87**, 106801 (2001)

[17] A. Bachtold, M. S. Fuhrer, S. Plyasunov, M. Forero, E. H. Anderson, A. Zettl, P. L. McEuen, Phys. Rev. Lett. **84**, 6082 (2000)

[18] P. Poncharal, C. Berger, Y. C. Yi, W. A. De Heer, Z. L. Wang, J. Phys. Chem. B **106**, 12104 (2002)

[19] C. T. White, T. N. Todorov, Nature **393**, 240 (1998)

[20] W. Liang, M. Bockrath, D. Bozovic, J. H. Hafner, M. Tinkham, M. Hongkun Park, Nature **411**, 665 (2001).

[21] P. J. Burke, IEEE Trans. Nanotech. **1**, 129 (2002).

[22] P. J. Burke, IEEE Trans. Nanotech. **2**, 55 (2003).

[23] C. L. Kane, T. C. Lubensky, T. C. R. Mukhopadhyay, Phys. Rev. Lett. **88**, (2002).

[24] D. V. Singh, K. A. Jenkins, J. Appenzeller, Electronics Lett. **41**, 280 (2005).

[25] A. Le Louarn, F. Kapche, J.-M. Bethoux, H. Happy, G. Dambrine, V. Derycke, P. Chenevier, N. Izard, M. F. Goffman, J.-P. Bourgoin, Appl. Phys. Lett. **90**, 233108 (2007).

[26] S. Rosenblatt, H. Lin, V. Sazonova, S. Tiwari, P. L. McEuen, Appl. Phys. Lett. **87**, 153111 (2005).

[27] Z. Yu, P. J. Burke, Nano Lett. **5**, 1403 (2005).

[28] J. J. Plombon, K. P. O'Brien, F. Gstrein, V. M. Dubin, Y. Jiao, Appl. Phys. Lett. **90**, 063106 (2007).

[29] C. Highstrete, E. A. Shaner, M. Lee, F. E. Jones, P. M. Dentinger, A. A. Talin, Appl. Phys. Lett. **89**, 173105 (2006).

[30] S. C. Jun, J. H. Choi, S. N. Cha, C. W. Baik, S. Lee, H. J. Kim, J. Hone, and J. M. Kim, Nanotech. **18**, (2007).

[31] P. Rice, T. M. Wallis, S. E. Russek, P. Kabos, Nano Lett. **7**, 1086 (2007).

[32] C. Rutherglen, D. Jain, P. Burke, Appl. Phys. Lett. **93**, 083119 (2008)

[33] Unidym, Inc., 1430 O'Brien Dr., Suite G, Menlo Park, CA 94025. URL: www.unidym.com.

[34] M. S. Arnold, A. A. Green, J. F. Hulvat, S. I. Stupp, M. C. Hersam, Nature Nanotech. **1**, 60 (2006).

[35] R. Krupke, F. Hennrich, H. v. Löhneysen, M. M. Kappes, Science **301**, 344 (2003).

[36] S. Soliveres, J. Gyani, C. Delseny, A. Hoffmann, F. Pascal, Appl. Phys. Lett. **90**, 082107 (2007).

[37] D. C. Look, D. C. Reynolds, J. R. Sizelove, R. L. Jones, C. W. Litton, G. Cantwell W. C. Harsch, Sol. St. Comm., **105**, 399 (1998)

[38] J. D. Albrecht, P. P. Ruden, S. Limpijumnong, W. R. L. Lambrecht, K. F. Brennan, J. Appl. Phys., **86**, 6864 (1999).

[39] Y.-J. Lee, T. L. Sounart, D. A. Scrymgeour, J. A. Voigt, J. W. P. Hsu, J. Crystal Growth, **304**, 80 (2007)

[40] R. B. Peterson, C. L. Fields, B. A. Gregg, Langmuir, **20**, 5114 (2004)

[41] E. D. Spoerke, M. T. LLoyd, Y.-J. Lee, B. B. Lambert, B. McKenzie, Y.-B. Jaing, D. C. Olson, T. L. Sounart, J. W. P. Hsu, J. A. Voight, J. Phys. Chem. C., published on line (2009)

Distribution

1	MS 0123	LDRD Office, 01030
1	MS 1415	Mark Lee, 01123
1	MS 1086	Clark Highstrete, 01123
1	MS 1415	Julia W.-P. Hsu, 01114
1	MS 1082	David Scrymgeour, 01725
1	MS 1086	Dan L. Barton, 01123
1	MS 1086	01123 Department File
1	MS 1415	Carlos Gutierrez, 01114
1	MS 1421	Jerry A. Simmons, 01120
1	MS 1071	C. Andy Boye, 01720
1	MS 1415	David R. Sandison, 01110
1	MS 1427	Julia M. Phillips, 01100
1	MS 1079	Gilbert V. Herrera, 01700
1	MS 0161	Patent and Licensing Office, 1150
1	MS 0899	Technical Library, 9536 (electronic copy)